
Truncated correlations in video microscopy of colloidal solids

Michael Schindler,^{*a} A.C. Maggs^a

Received Xth XXXXXXXXXXXX 20XX, Accepted Xth XXXXXXXXXXXX 20XX

First published on the web Xth XXXXXXXXXXXX 20XX

DOI: 10.1039/b000000x

Studies by video microscopy on fluctuating colloids measure the real-space cross-correlations in particle motion. This set of correlations is then treated as a matrix, in order to study the spectrum and mode structure. We show that in general the modes are modified by the truncation of the full real-space correlations. We perform a theoretical analysis of the truncation, find the boundary conditions imposed by the truncation, and propose practical windowing strategies to eliminate artefacts. We study the problem from various perspectives, to compile a survey for experimentalists.

1 Introduction

Many experiments have studied the fluctuations of two and three dimensional colloidal solids (both crystalline, amorphous and glassy) using video and confocal microscopy¹⁻⁹. A section of a large sample is observed and recorded; fluctuations of the subsystem are then analysed off-line. In particular one wishes to measure the mode structure and dispersion relations of the medium to extract material properties such as elastic constants. An important technical question which comes up is how to perform analysis on data which is gathered within a window which is smaller than the full sample. One of the main reasons for working with such truncated data is of course the hope of eliminating the uncontrolled influence of walls by imaging well within the sample using confocal techniques. We will show, however, that truncating the full set of fluctuations outside of the observation window introduces effective boundary conditions which rather unexpectedly lead to errors in measurements of material properties.

The crucial question is how the result of the observed mode structure converges when the observation volume increases. It is generally assumed that convergence is assured for large system size. After all, Weyl's theorem on the density of states of a vibrating system shows that the density of states is asymptotically independent of the system shape¹⁰; thus theorists freely interchange the true boundary conditions of a physical system by a mathematically convenient choice of periodic modes. However, we show in this paper that the assumption is dangerous when using Fourier analysis of observed amplitudes. To be concrete let us now summarize the kinds of data and analysis which are available:

Video or confocal observation of colloidal solids generates data sets consisting of the position of particles recorded over many frames. One then calculates the mean position of each

particle and the correlations in the displacements, $u_i(\mathbf{r})$, by evaluating the two-particle function

$$C_{ij}(\mathbf{r}, \mathbf{r}') = \langle u_i(\mathbf{r})u_j(\mathbf{r}') \rangle \quad (1)$$

with directional indexes i, j , and with \mathbf{r} being the reference positions of the N particles. The average is over the recorded frames. We work in d -dimensional space where the interesting values are $d = 2, 3$ when imaging colloids at interfaces, or within volumes.

Three methods of analysis suggest themselves:

- (A) diagonalisation of the correlation matrix eq. (1) of dimension $(dN) \times (dN)$ in order to study its eigenvalues and eigenvectors,
- (B) evaluation of amplitudes in Fourier space*

$$u_i(\mathbf{q}) = \sum_{\mathbf{r}} e^{i\mathbf{q}\cdot\mathbf{r}} u_i(\mathbf{r}), \quad (2)$$

followed by a similar study of the matrix

$$C_{ij}(\mathbf{q}, \mathbf{q}') = \langle u_i(\mathbf{q})u_j(\mathbf{q}') \rangle, \quad (3)$$

- (C) direct use of only the diagonal Fourier coefficients

$$C_{ij}(\mathbf{q}, -\mathbf{q}) = \langle u_i(\mathbf{q})u_j(-\mathbf{q}) \rangle \quad (4)$$

which reduces, for a Bravais lattice, to a set of N matrices of size $d \times d$.

The full diagonalisation of the matrix C_{ij} allows one to plot *visually seductive* pictures of mode structure in the truncated system. The question arises as to the *exact* link between these plots and the standard treatment of modes in an elastic medium

^a Laboratoire PCT, Gulliver CNRS-ESPCI UMR 7083, 10 rue Vauquelin, 75231 Paris Cedex 05.

* We differentiate in notation between the reciprocal vectors of the full (possibly infinite) system, \mathbf{k} , and \mathbf{q} for those of the windowed system.

via the wave equation. In particular are there effective boundary conditions introduced by the truncation which influence the modes? In this paper we show that in a simple square geometry eigenmodes of the correlation matrix do not have a pure longitudinal or transverse nature, unlike a bulk sample. We quantify this effect in a study of a two-dimensional elastic medium. We also note that the decomposition into longitudinal and transverse is in ambiguous in finite geometries.

The second formulation in terms of a matrix of Fourier coefficients requires some care as to the definition of the eigenvalue problem in order to be equivalent to the real space form¹¹, in particular in a disordered system plane waves do not form an orthonormal basis; thus one must study a generalized, pencil eigenvalue problem. We will not consider this case further in the present paper.

The use of the third method, studying $C_{ij}(\mathbf{q}, -\mathbf{q})$ seems particularly practical in large experimental systems because it avoids the expensive diagonalisation that is required for the other two cases. It might be expected to give exact results for elastic moduli in crystals, and good estimates in disordered, non-glassy solids. However, we will show numerically that $C_{ij}(\mathbf{q}, -\mathbf{q})$ is contaminated by the truncation of the full correlation functions. We explain the result visually with an analogy with the diffraction pattern of the observation window. We propose a simple practical solution to the contamination by the use of alternative windowing functions with superior properties in Fourier space.

2 Elastic theory

In this section we resume the results from elasticity theory that we will require. In a three-dimensional elastic medium the quadratic fluctuations about the energy minimum, as well as the propagating modes of a crystal are deduced from the Christoffel matrix¹². In a cubic solid this has the form

$$D_{ik}(\mathbf{k}) = \left[\lambda \delta_{ij} \delta_{kl} + \mu (\delta_{ik} \delta_{jl} + \delta_{il} \delta_{jk}) + \nu S_{ijkl} \right] k_j k_l, \quad (5)$$

with Lamé constants λ , μ and anisotropy ν . This expression is also valid under uniform, isotropic stress such as the pressure which must be applied in non-bound colloidal solids. The free energy of small fluctuations about the equilibrium position is then given by the functional

$$E[\mathbf{u}] = \sum_{i,j,\mathbf{k}} \frac{1}{2} u_i(\mathbf{k}) u_j(-\mathbf{k}) D_{ij}(\mathbf{k}). \quad (6)$$

The Green function of the static elastic problem is then the inverse of the Christoffel matrix,

$$D_{ij}(\mathbf{k}) G_{jk}(\mathbf{k}) = \delta_{ik}. \quad (7)$$

It describes the response of the medium to static forces, as well as correlations in position fluctuations which can be measured

in microscopy. In a face-centred cubic crystal with nearest-neighbour central potentials $\mu = \lambda = -\nu$, see Eq. (12.7) of Ref. 13. Face-centred hard-sphere systems and real experiments have non-linearities that slightly modify the relation between these three constants¹⁴.

A similar mathematical structure describes fluctuations in a two-dimensional hexagonal crystal, with however $\nu = 0$, implying that the long-wavelength mode structure is isotropic with just two types of modes- longitudinal and transverse. This theory can be used to study the statistics of colloidal crystals at interfaces⁵.

For many of the discussions in this paper the most important characteristic of the matrix eq. (5) is the scaling in k^2 . This motivates the study of a scalar energy function

$$E[u] = \frac{\lambda}{2} \int (\nabla u)^2 d\mathbf{r} = \frac{\lambda}{2} \sum_{\mathbf{k}} k^2 |u(\mathbf{k})|^2. \quad (8)$$

Such energy functions eliminate the need for detailed tensor analysis and allow one to transpose well known theorems in potential theory to our study of truncation artefacts. In particular for eq. (8) we find

$$G(\mathbf{k}) = \frac{1}{\lambda k^2}. \quad (9)$$

Then the real-space Green (in $d = 3$) function is given by the Fourier transform of eq. (9)

$$G(\mathbf{r} - \mathbf{r}') = \int e^{i\mathbf{k} \cdot (\mathbf{r} - \mathbf{r}')} G(\mathbf{k}) \frac{d\mathbf{k}}{(2\pi)^d} = \frac{1}{4\pi\lambda |\mathbf{r} - \mathbf{r}'|}. \quad (10)$$

The correlations are translationally invariant. The corresponding correlations for isotropic elasticity can be found in standard references¹⁵, again the decay in separation varies as $1/|\mathbf{r} - \mathbf{r}'|$, with additional tensor structure. Expressions with cubic anisotropy are treated in the recent literature¹⁶. The experimental correlation matrices are related via equipartition to the Green function:

$$\langle u_i(\mathbf{k}) u_j(-\mathbf{k}) \rangle = k_B T G_{ij}(\mathbf{k}), \quad (11)$$

where the correlation is evaluated for the full system and not truncated to a window.

Experimentalists also study *projected* correlations, rather than the full three-dimensional problem. The experiments thus determine a slice of the full correlation matrix. In this case we need to determine the effective energy function of the sliced system. It can be shown^{6,17} that projection from d to $d - 1$ dimensions changes the dispersion law in elastic theory from \mathbf{k}^2 to $|\mathbf{k}_\perp|$ where \mathbf{k}_\perp is a wave vector in the projected space and \mathbf{k} is the wave vector in the starting space.

3 Corruption of correlations by truncation

To demonstrate the problem of working with only the diagonal elements $C_{ij}(\mathbf{q}, -\mathbf{q})$ in truncated data (method (C) in the introduction) we here present results of molecular dynamics simulations performed in two dimensions on a hexagonal crystal of hard spheres using event driven methods¹⁸. In Fig. 1a, we have analysed the mode structure of the whole, periodic, system. As noted above the long-wavelength mode structure is described by two elastic constants, λ , μ and there is rotational invariance in long-wavelength correlations. In the figure this results in there being just two independent intersects for small wave vectors when we plot ω/k as a function of k . Here $\omega^2(\mathbf{k})$ is defined as the eigenvalues of the 2×2 matrix $G_{ij}(\mathbf{k})$ for a given vector \mathbf{k} . For the full simulation volume we conclude that we are able to extract the effective elastic properties from the diagonal values $C_{ij}(\mathbf{k}, -\mathbf{k})$. Eq. (11) therefore holds.

However, observation of the data in a finite observation window leads to considerable modifications in the result, Fig. 1b. We observe a breakdown in rotational invariance, as shown by the splitting of previously degenerate modes at small wave vectors. In addition the situation does not improve on increasing the system size. The main point of the first part of the present paper is understanding the result of Fig. 1b analytically and finding analytic and numerical methods which allow one to restore the correct symmetries to the data, in order to correctly characterize experimental systems and simulation data.

In Fig. 2 we have performed similar analysis of a three-dimensional simulation. The results in panel (a) are more complicated than in two dimensions because of the influence of cubic anisotropy. But one clearly sees that the very highest mode in panel (a) is displaced to lower ω in panel (b), leading to important modifications in the effective elastic properties that one would deduce from the data.

We must conclude that truncating data in a larger experimental system does not lead to a satisfactory method for measuring elastic properties. We now demonstrate analytically the origin of the problem.

3.1 Windowing theory

Let us window the data of an experiment or simulation to a region w and consider the general two-wavevector transform

$$G_w(\mathbf{q}, \mathbf{q}') = \int_w \int_w e^{-i(\mathbf{q}\mathbf{r} + \mathbf{q}'\mathbf{r}')} G(\mathbf{r}, \mathbf{r}') d\mathbf{r} d\mathbf{r}', \quad (12)$$

where the integrals are over the observation window. We generalize by considering a weighting function $W(\mathbf{r})$ which is an arbitrary positive function. We will always normalize this function such that

$$\int W^2(\mathbf{r}) d\mathbf{r} = \int |W(\mathbf{k})|^2 \frac{d\mathbf{k}}{(2\pi)^d} = 1. \quad (13)$$

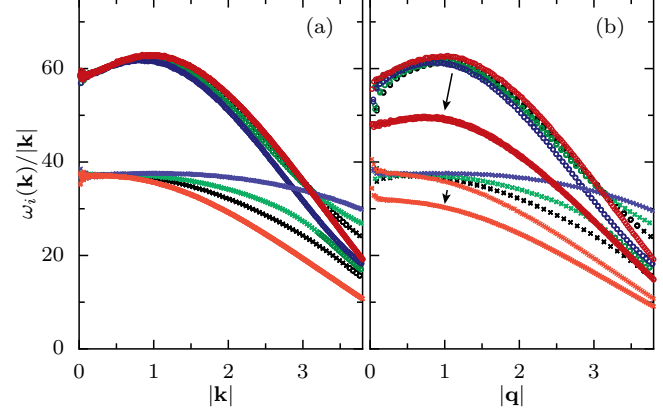


Figure 1 Windowing artefacts in two-dimensional data. (a) Molecular dynamics data for a hexagonal crystal, analysed for its mode structure in periodic boundary conditions. For small wave vectors k we see just two branches corresponding to longitudinal (upper, dark) and transverse (lower, light) modes. (b) The data is extracted from an observation window, half the system size in both directions, analysed in the same way, plotted are $\omega_i(\mathbf{q})/|\mathbf{q}|$. The modes split and symmetry-related directions are no-longer equivalent. Note windows have non-square shape adapted to the underlying hexagonal lattice

We find in Fourier space that

$$G_w(\mathbf{q}, \mathbf{q}') := \int W(\mathbf{q} - \mathbf{k}) W(\mathbf{k} + \mathbf{q}') G(\mathbf{k}) \frac{d\mathbf{k}}{(2\pi)^d}. \quad (14)$$

Windowing to a cube corresponds to a constant $W(\mathbf{r})$ within the observation zone so that $W(\mathbf{k})$ can be expressed in terms of the sinc function, well known from the theory of diffraction.

$$W(\mathbf{k}) = L^{d/2} \prod_{i=1}^d \text{sinc}\left(\frac{k_i L}{2}\right), \quad (15)$$

where the product is over the number of dimensions. This type of window will be analysed in detail below.

We would hope that in the limit of large windows the matrix $G_w(\mathbf{q}, -\mathbf{q}')$ is dominated by its diagonal elements and resembles *in some sense* $G(\mathbf{k})$, thus $W(\mathbf{k})$ should act as a δ -function. We now examine the conditions in which this happens. To understand the failures of Fig. 1b let us look at an estimate for the diagonal elements $G_w(\mathbf{q}, -\mathbf{q})$. We consider the scalar theory with $G = 1/\lambda k^2$. Then

$$G_w(\mathbf{q}, -\mathbf{q}) = \int |W(\mathbf{k} - \mathbf{q})|^2 \frac{1}{\lambda k^2} \frac{d\mathbf{k}}{(2\pi)^d}. \quad (16)$$

$|W(\mathbf{k})|^2$ is simply the Fraunhofer diffraction intensity of the measurement window.[†]

[†] The cosine or sine transforms of the correlations can similarly be expressed in terms the combinations $[G_w(\mathbf{q}, -\mathbf{q}) \pm G_w(\mathbf{q}, \mathbf{q})]$.

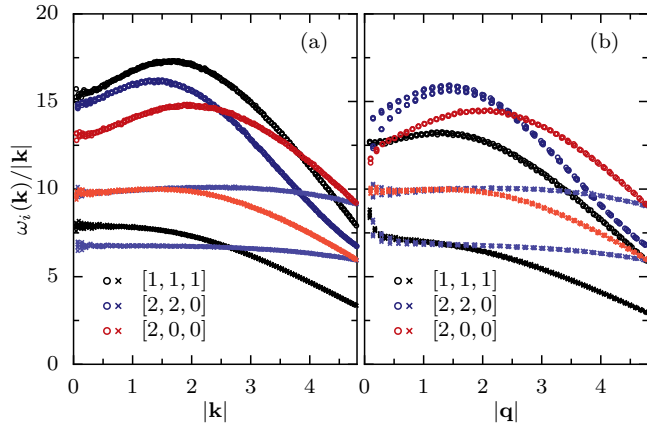


Figure 2 As for Fig. 1 but for three-dimensional analysis. While the modification of the mode structure is less drastic than in two dimensions the longitudinal structure is significantly different in the original and windowed data sets.

3.1.1 Gaussian window Explicit progress can be made using (idealized) Gaussian windows with

$$W(\mathbf{r}) = \frac{1}{(\pi\sigma^2)^{d/4}} e^{-\mathbf{r}^2/2\sigma^2}, \quad (17)$$

$$W(\mathbf{k}) = (4\sigma^2\pi)^{d/4} e^{-\sigma^2\mathbf{k}^2/2}. \quad (18)$$

where σ is a measure of the real-space width of the window. Potentially large contributions to the integral in eq. (16) can come from the central peak of $W(\mathbf{k}-\mathbf{q})$ for $\sigma|\mathbf{k}-\mathbf{q}| = \mathcal{O}(1)$, or from the divergence of $G(\mathbf{k})$ at $k = \mathbf{0}$. However the very rapid decay of $W(\mathbf{k})$ implies that the contribution of the integral from $k = \mathbf{0}$ is very small if $\sigma q \gg 1$. We perform the integral in eq. (16) with a Gaussian window and find

$$G_w(\mathbf{q}, -\mathbf{q}) = e^{-q^2\sigma^2} \frac{\sqrt{\pi}\sigma}{\lambda q} \operatorname{erfi}(\sigma q), \quad (19)$$

With erfi the imaginary error function. When z is small, $\operatorname{erfi}(z) \approx 2z/\sqrt{\pi}$, implying that

$$G_w(\mathbf{q}, -\mathbf{q}) = \frac{2\sigma^2}{\lambda} \quad \text{for } \sigma q \text{ small.} \quad (20)$$

When z is large $e^{-z^2} \operatorname{erfi}(z) \approx 1/\sqrt{\pi}(z^{-1} + z^{-3}/2)$, so that

$$G_w(\mathbf{q}, -\mathbf{q}) = \frac{1}{\lambda q^2} \left[1 + \frac{1}{2(\sigma q)^2} + \dots \right] \quad \text{for } \sigma q \text{ large.} \quad (21)$$

Thus with this well-behaved windowing function $G_w(\mathbf{q}, -\mathbf{q})$ does indeed converge to the desired limit, $G(\mathbf{q})$, where corrections are higher order in $1/\sigma q$. While for very small values of σq the Gaussian window leads to an overestimate of the

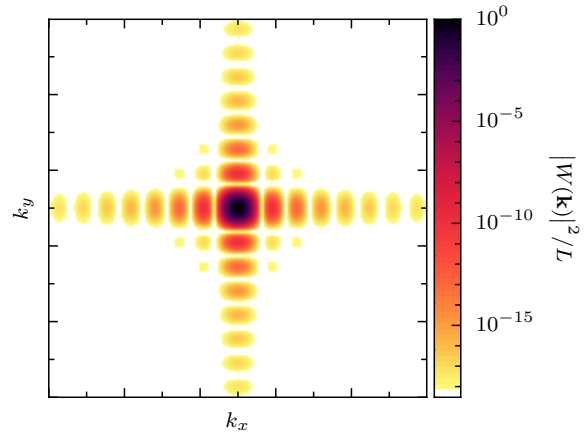


Figure 3 Fourier transform, $|W(\mathbf{k})|^2$, of the weighting function for a square sampling window, eq. (15). Perpendicular to each side of the window the asymptotic decay of the function is slow, $1/k^2$. The decay in general directions is faster, $1/k^4$. The slow decay along the symmetry directions leads to major artefacts in the reconstructed spectrum.

elastic modulus, for most reasonable values of the parameter we expect a small underestimate in the elastic modulus. The theory of windowing with a tensorial Green function is given in Appendix A where we show that we obtain the correct answer for the both the longitudinal and transverse modes in an isotropic medium when σq large.

3.1.2 Discontinuous windows We now return to the windowing function eq. (15) which corresponds to truncating the data. We plot the diffraction intensity for a two-dimensional square in Fig. 3. One sees that the diffraction pattern is characterized by a notable “cross”-structure in the directions $(1,0)$ and $(0,1)$. In these two directions the envelope of Fourier coefficients decays slowly as $1/k^2$, while off axis the decay is faster, $1/k^4$. We now show that the decay in $1/k^2$ leads to convergence of the integral in eq. (16) to an incorrect value and is the origin of the breakdown in rotational invariance in Fig. 1. The splitting that occurs in Fig. 1 indeed corresponds to corruption of modes which are parallel to the slowly decaying directions in the diffraction pattern of the truncating box. A third mode in the figure, which is equivalent by symmetry of the hexagonal lattice but not of the windowing function, remains unaffected by truncation. Note that such high symmetry directions are those that are the most natural to analyse in an experimental setup. The problem is that this diffraction pattern with envelope $1/k^2$ is not sufficiently “close” to a δ -function. Qualitatively we see that we are trying to extract a signal with a power spectrum in $1/k^2$ with a discontinuous function which has the same power spectrum.

We now argue quantitatively by estimating the integral eq. (16) with the weighting function of Fig. 3. Again two

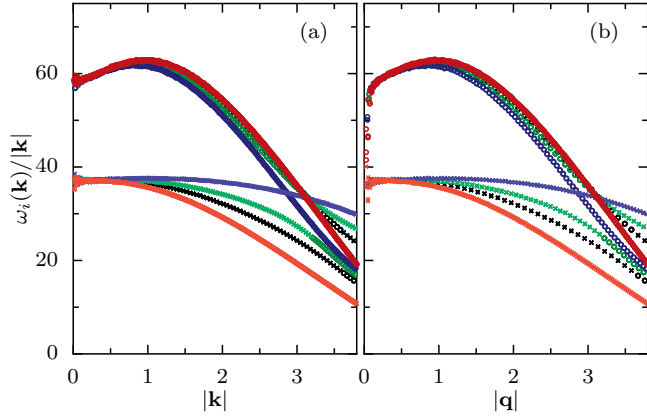


Figure 4 As Fig. 1 but using a Hann window in (b). The windowing artefacts are largely eliminated, but the longest wavelength modes are modified due to mode mixing. See Appendix A. Skew window adapted to simulation box.

potentially large contributions come in the neighbourhood of $\mathbf{k} = \mathbf{0}$ and $\mathbf{k} = \mathbf{q}$. For the integral near $\mathbf{k} = \mathbf{q}$, the normalization of W is designed so that the contribution is exactly that corresponding to the physical values of G . It is the ball around $\mathbf{k} = \mathbf{0}$ that is particularly problematic, it gives a second, non-negligible contribution to the integral. With the natural choice of wave vectors $q_i = 2\pi n/L$ the pole at $\mathbf{k} = \mathbf{0}$ is placed on a zero of the diffraction pattern, however the contribution of a ball of size $\Delta k \sim 1/L$ includes the nearby maxima of the diffraction pattern. The envelope of $|W(\mathbf{k}-\mathbf{q})|^2$ is slowly varying and can be replaced by a typical value $L^d/(qL)^2$. In the x -direction we have $|W(\mathbf{k}-\mathbf{q})|^2 \sim |W(\mathbf{q})|^2(k_x L)^2$ and find the contribution the contribution of the ball,

$$|W(\mathbf{q})|^2 \int_0^{1/L} (k_x L)^2 \frac{k^{d-1} dk}{\lambda k^2} = \frac{L^{d-2}}{\lambda q^2} \int_0^{1/L} \frac{k^{d-1} dk}{k^2} \sim \frac{1}{\lambda q^2}. \quad (22)$$

This contribution adds to the $\mathcal{O}(1/\lambda q^2)$ contribution near $\mathbf{k} = \mathbf{q}$. The sinc window over-estimates G , and thus naturally underestimates effective elastic moduli. In Fig. 1b the dispersion curves which are perpendicular to the window limits are indeed lower than the correct values.

3.2 Improved weighting functions

A detailed study of the spectrum properties of windows in signal processing is given by Nuttall¹⁹. We see that the (unrealisable) Gaussian window has excellent properties due to the suppression of the contribution of the integral at $\mathbf{k} = \mathbf{0}$. Sinc-like windows are inadequate due to their slow decay in Fourier space. We now show that a product of Hann windows

$$W(x) = (1 + \cos 2\pi x/L), \quad -L/2 \leq x \leq L/2, \quad (23)$$

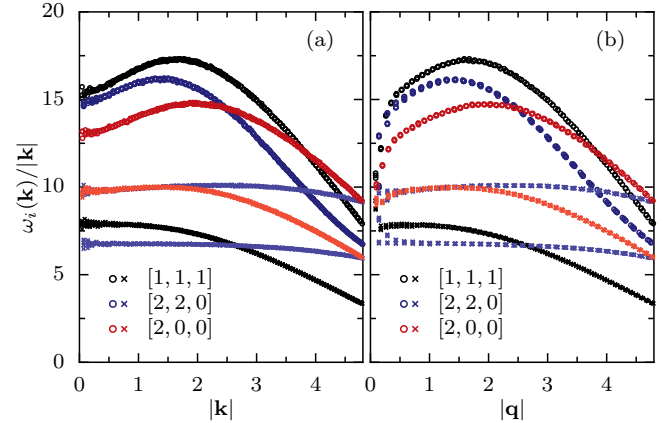


Figure 5 As Fig. 2 but using a Hann window in (b). The windowing artefacts are largely eliminated, but the longest wavelength modes are modified due to mode mixing, compare Appendix A. Skew window adapted to simulation box.

has superior Fourier properties. We find

$$W(k) \sim 2 \operatorname{sinc}(kL/2) + \operatorname{sinc}(kL/2 - \pi) + \operatorname{sinc}(kL/2 + \pi), \quad (24)$$

for which at large wave vectors $|W(k)|^2 \sim 1/k^6$. Such a rapidly decaying function behaves as a δ -function when tested against a Green function in $1/k^2$.

We reanalysed our two-dimensional data in Fig. 4 using this Hann window and find greatly improved results, including restoring of rotational invariance in the data. If one repeats the analysis of contributions to G_w coming from $k = 0$ one sees that they are now sub-dominant. One can trust the results to reconstruct the true dispersion law.

The corresponding results in three dimension are given in Fig. 5. We note that results for the longitudinal modes drop sharply for small q , while the transverse modes rise. We give a theory of this effect in Appendix A where we analyse the problem of Gaussian windowing in three dimensional isotropic media. We show that it is due to a mixing of longitudinal and transverse modes which occurs for small wavevectors and corrupts the dispersion relation. Note this is an effect which only occurs for a few low-lying modes- in distinction to the problems with sharp windows which lead to all modes in certain directions being corrupted.

3.3 Observation of slices and projection

What is the situation in projection geometries where the effective dispersion law is $G(\mathbf{k}) \sim 1/|k|$, cf. Refs. 6,17? Here the use of a sinc-function indeed reproduces the wanted leading term in $1/|q|$ with the correct prefactor, the integral near

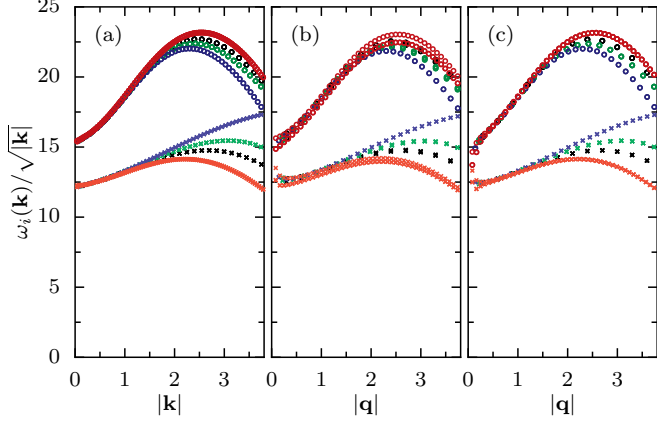


Figure 6 Projected dispersion curves from the simulation in Fig. 2. The projected system is two-dimensional and isotropic. (a) full system, (b) truncation window, (c) window with Hann weighting functions, see eq. (23).

$\mathbf{k} = \mathbf{q}$ is however less divergent than in the case treated above, so that the origin contributes a sub-leading correction in $1/q^2$. At least asymptotically the correct dispersion relation is observed in $G_w(\mathbf{q}, -\mathbf{q})$, though with a leading correction which can no-doubt be improved with the use of a windowing function which falls to zero at the edge of the observation zone. We did indeed simulations to test this point and found the correct reconstructed dispersion law, Fig. 6.

3.4 Off-diagonal elements

For the ideal case of the Gaussian window one can estimate the off-diagonal equivalent to eq. (21). Via a saddle point calculation we find

$$G_w(\mathbf{q}, -\mathbf{q}') \approx \frac{4}{(\mathbf{q} + \mathbf{q}')^2} e^{-\sigma^2(\mathbf{q} - \mathbf{q}')^2/4}. \quad (25)$$

Higher order corrections can also be calculated. An interesting, but difficult, problem would be to solve for the eigenvalue structure of this effective matrix.

4 Mode structure of the full correlation matrix

We now turn to study of the full correlation matrix $C_{ij}(\mathbf{r}, \mathbf{r}')$ of a truncated system, method (A) in the introduction. An experimentalist first measures a set of correlation functions and assembles them into such a matrix. It is then natural (and easy with tools such as Matlab) to study the eigenvectors of this matrix. How are the eigenvectors in a truncated system related to those of the underlying physical system which is described in terms of elastic properties? We wish to relate the eigenvalues and eigenvectors of this matrix in the limit

of small wave vectors to those from a true continuum theory in unbounded space. The particular questions that we study include the effective boundary conditions for eigenfunctions that arise from the truncation. We will make particular use of the scalar analogue of elasticity to simplify the analytic calculations and to display relevant features of the mathematical problem. We find the exact analytic solution to the scalar problem in spherical and circular geometries but use numerical methods in square geometries. We find the quantisation conditions by direct study of the duplicating property of an integral operator, and we show that simple Neumann and Dirichlet boundary conditions do not give the correct mode structure.

4.1 Scalar elasticity

We have noted that the problem of scalar elasticity is linked to the properties of the Laplacian operator which corresponds to the Helmholtz eigenvalue equation:

$$[\nabla^2 + k^2]\psi = 0, \quad (26)$$

The correlation matrix from scalar elasticity is then the form $C(\mathbf{r}, \mathbf{r}') = 1/4\pi|\mathbf{r} - \mathbf{r}'|$.

If we construct a (continuum) matrix from the correlations we are thus interested in the following integral equation

$$\int_V \frac{1}{4\pi|\mathbf{r} - \mathbf{r}'|} \psi(\mathbf{r}) d^3\mathbf{r} = \Lambda\psi(\mathbf{r}'), \quad (27)$$

The eigenvalue is Λ , and we are restricted to a finite volume $V \subset \mathbb{R}^3$. The mathematical difficulty comes from the arbitrary choice for the shape of V .

Consider equation eq. (27) with \mathbf{r}' within the observation volume then we can act on this equation with $-\nabla^2$ acting on the \mathbf{r}' coordinate to find

$$\int_V \delta(\mathbf{r} - \mathbf{r}') \psi(\mathbf{r}) d^3\mathbf{r} = \psi(\mathbf{r}') = -\Lambda\nabla^2\psi(\mathbf{r}'), \quad (28)$$

which is the Helmholtz equation with eigenvalue $\Lambda = k^{-2}$. Thus the matrix of correlation functions has eigenvectors ψ_k which are closely related to those of the corresponding differential equation, however we will now show that the boundary conditions are different. We have the equations

$$-\nabla^2 G(\mathbf{r} - \mathbf{r}') = \delta(\mathbf{r} - \mathbf{r}'), \quad (29)$$

$$(\nabla^2 + k^2)\psi_k(\mathbf{r}) = 0. \quad (30)$$

Multiplying eq. (29) by $\psi_k(\mathbf{r})$ and eq. (30) by $G(\mathbf{r} - \mathbf{r}')$ leads to

$$\int_V d\mathbf{r} [\psi_k \nabla^2 G - G \nabla^2 \psi_k - k^2 \psi_k G] = -\psi_k(\mathbf{r}'). \quad (31)$$

Using Green's second identity we find

$$\oint_{\partial V} d\mathbf{S}_r \cdot [\psi_k \nabla G - G \nabla \psi_k] = -\psi_k(\mathbf{r}') + k^2 \int_V d\mathbf{r} \psi_k(\mathbf{r}) G(\mathbf{r}, \mathbf{r}').$$

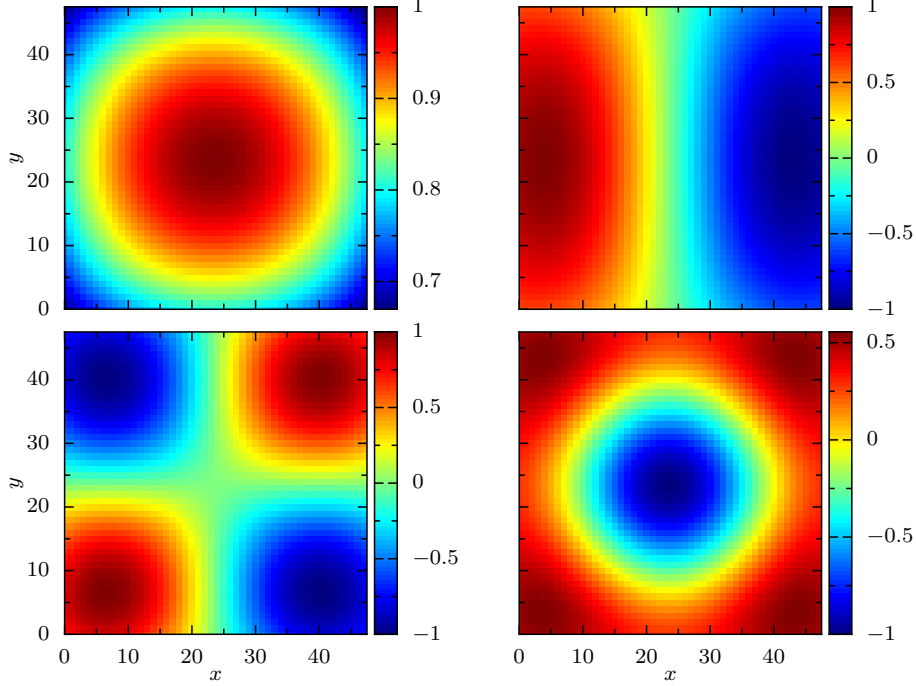


Figure 7 Amplitudes of modes found in a square observation window 48×48 pixels, using scalar elasticity. Top left to bottom right decreasing eigenvalues of the integral operator. Note that first mode is not constant within the observation volume despite it being the most uniform mode. The second mode displays a noticeable non-sinusoidal form.

We recognize the right-hand side as the eigenvalue equation in integral form, thus the condition

$$\oint_{\partial V} d\mathbf{S}_r \cdot [\psi_k(\mathbf{r}) \nabla G(\mathbf{r}, \mathbf{r}') - G(\mathbf{r}, \mathbf{r}') \nabla \psi_k(\mathbf{r})] = 0 \quad \forall \mathbf{r}' \quad (32)$$

is required for ψ_k being an eigenmode both of the elastic problem (26) and of the truncated integral equation (27). For any eigenvector ψ_k , this is a set of integral conditions, true for each interior point \mathbf{r}' . In spherically symmetric domains V , see Sec. 4.3 below, they reduce to boundary conditions valid on the surface. In the general case, this cannot be assumed to be the case.

4.2 Tensor elasticity

While performed in the simplest scalar form, the above theory can be easily replaced by its tensorial equivalent for an elastic medium. The only difference is the use of Betti's identity for the stress tensor rather than Green's second theorem²⁰. Let

$$\Delta_{ik}^* := C_{ijkl} \partial_j \partial_l \quad \text{in general, and} \quad (33)$$

$$\Delta^* = (\lambda + \mu) \text{grad div} + \mu \nabla^2 \quad \text{if isotropic,} \quad (34)$$

then

$$\oint_{\partial V} dS [(\partial_N G) \cdot \mathbf{u} - G \cdot (\partial_N \mathbf{u})] = \int_V [(\Delta^* G) \cdot \mathbf{u} - G \cdot (\Delta^* \cdot \mathbf{u})] d\mathbf{r} \quad (35)$$

with $\partial_N \mathbf{u}$ the normal stress and $\partial_N G$ the normal derivative of the Green function,

$$\partial_N := C_{ijkl} \partial_j N_l. \quad (36)$$

The truncated and the elastic eigenvalue problems then have the same eigenfunctions if the integral relation

$$\oint_{\partial V} dS [(\partial_N G) \cdot \mathbf{u} - G \cdot (\partial_N \mathbf{u})] = \mathbf{0} \quad (37)$$

holds for any eigenvector \mathbf{u} and for any point \mathbf{r}' (the integrals and derivatives in eqs. (33)–(37) act on \mathbf{r}).

4.3 Scalar spherically symmetric solutions

We now derive the exact quantization conditions in rotationally symmetric geometries, again studying the scalar vibrational problem: Regular solutions to the Helmholtz equation in spherically symmetric geometries can be written in terms of spherical Harmonics Y_l^m and spherical Bessel functions j_l ,

$$\Psi_l^m(\mathbf{r}) = j_l(kr) Y_l^m(\Omega). \quad (38)$$

$\Omega = (\theta, \phi)$ is a solid angle in spherical polar coordinates. For $l = 0$ we note that

$$\Psi_0^0 = j_0(kr) = \frac{\sin(kr)}{kr}. \quad (39)$$

Let us show that Ψ_l^m is also a solution to the truncated integral equation (27) for correct choices of k .

As domain we consider the ball of radius R around the origin, $V = B_R(\mathbf{0})$, so that the integral operator acting on the trial function is given by

$$I = \int_{B_R(\mathbf{0})} \frac{1}{4\pi|\mathbf{r}-\mathbf{r}'|} \Psi_l^m(\mathbf{r}) d^3\mathbf{r}. \quad (40)$$

We use the identity ($r_{<} = \min(r, r')$ and $r_{>} = \max(r, r')$)

$$\frac{1}{|\mathbf{r}-\mathbf{r}'|} = \sum_{l=0}^{\infty} \sum_{m=-l}^l \frac{r_{<}^l}{r_{>}^{l+1}} \frac{4\pi}{2l+1} (-1)^m Y_l^m(\Omega) Y_l^{-m}(\Omega')$$

to break the integral into a radial and an angular part, and then use the fact that after the angular integrals only a single spherical harmonic survives so that we must evaluate

$$I = \frac{Y_l^m}{2l+1} \int_0^R \frac{1}{|\mathbf{r}-\mathbf{r}'|} j_l(kr) \frac{r_{<}^l}{r_{>}^{l+1}} r^2 dr. \quad (41)$$

We explicitly split the integration to find

$$I = \frac{Y_l^m}{2l+1} \left(\int_0^{r'} \frac{r'^{l+2}}{r'^{l+1}} j_l(kr) dr + \int_{r'}^R \frac{r'^l}{r'^{l-1}} j_l(kr) dr \right).$$

We now use the identities²¹

$$\int z^{n+1} j_{n-1}(z) = z^{n+1} j_n(z), \quad (42)$$

$$\int \frac{1}{z^n} j_{n+1}(z) = -\frac{1}{z^n} j_n(z), \quad (43)$$

$$j_{n+1}(z) + j_{n-1}(z) = \frac{(2n+1)}{z} j_n(z), \quad (44)$$

to transform the integrals into

$$I = \frac{Y_l^m(\Omega')}{k^2} \left(j_l(kr') - \frac{j_{l-1}(kR)}{2l+1} \frac{(kr')^l}{(kR)^{l-1}} \right). \quad (45)$$

This is of the original form Ψ_l^m if $j_{l-1}(kR) = 0$ which serves to obtain possible values for k :

$$l = 0: \quad \cos(kR) = 0 \quad \Rightarrow \quad kR = (n+1/2)\pi, \quad (46)$$

$$l = 1: \quad \sin(kR) = 0 \quad \Rightarrow \quad kR = n\pi, \quad \text{etc.} \quad (47)$$

The condition $z j_{l-1}(z) = 0$ can be reformulated as²¹

$$z \frac{d}{dz} j_l(z) + (l+1) j_l(z) = 0, \quad \text{with } z = kR, \quad (48)$$

which is a mixed (Robin) boundary condition for Ψ_l^m on the sphere. Now we understand how we change the original elastic problem (26) if we truncate the domain: Truncating is

equivalent to applying the boundary conditions (48) to the different solutions of eq. (26). Note that for different l we have different boundary conditions.

A very similar expansion in ($r_{<}/r_{>}$) can be performed in two dimensions for a disk, where the eigenfunctions $e^{im\theta} J_m(kr)$ give rise to the eigen-equation $J_{m-1}(kR) = 0$ for $m > 0$. For $m = 0$ the corresponding equation is

$$J_0(z) + z \log(z/z_0) J_1(z) = 0, \quad (49)$$

with $z = kR$ and z_0 a reference radius.

4.4 Square geometry

We were unable to solve the integral equation eq. (27) in the geometry of a square or cubic box. We thus proceed by numerical investigation. We generate the Green function in a large, periodic box of dimension 500×500 using fast Fourier transforms¹⁷. We then truncate the Green function to a window of dimension 48×48 . This Green function is then diagonalized using standard dense algebra packages included in Matlab. The structure of the modes that is found is demonstrated in Fig. 7. The simplest mode (top left panel) has a largely constant amplitude over the observation region, it does have a gentle peak at the centre, however, which is some 30% higher than the value of the function in the corners. It is interesting to note that this mode has finite energy- it does not correspond to a zero mode of the Helmholtz system. The next mode (top right panel), which is two-fold degenerate, has the nature of a wave within the box. However we see that it is definitely non-sinusoidal and the contours of constant amplitude bow out at the edge of the observation volume.

The methods generalize to vector elasticity in two dimensions. We use a modification of the method of Ref. 17 to generate a discretised version of the matrix D in eq. (5), with $\mathbf{v} = 0$. In particular we choose a discretised dispersion relation

$$D(\mathbf{k}) = \mu(4 - 2\cos k_x - 2\cos k_y) \begin{pmatrix} 1 & 0 \\ 0 & 1 \end{pmatrix} + (\lambda + \mu) \begin{pmatrix} 2 - 2\cos k_x & \sin k_x \sin k_y \\ \sin k_x \sin k_y & 2 - 2\cos k_y \end{pmatrix} \quad (50)$$

and use the fast Fourier transform to generate the corresponding real-space form $G_{ij}(\mathbf{r})$. We truncate this Green function to a square and diagonalize. The dispersion relation differs from our previous choice¹⁷ and has the advantage of preserving more properties of the continuum elastic theory that we wish to study. In particular our previous choice leads to a subdominant contribution to the $G_{xy}(\Delta x, 0)$. In our previous work it decays as $1/(\Delta x)^2$ for large separations Δx . The new form eq. (50) gives zero for this quantity.

In the leftmost column of fig. 8 we plot the vector displacement fields of three of the lower eigenmodes in an isotropic

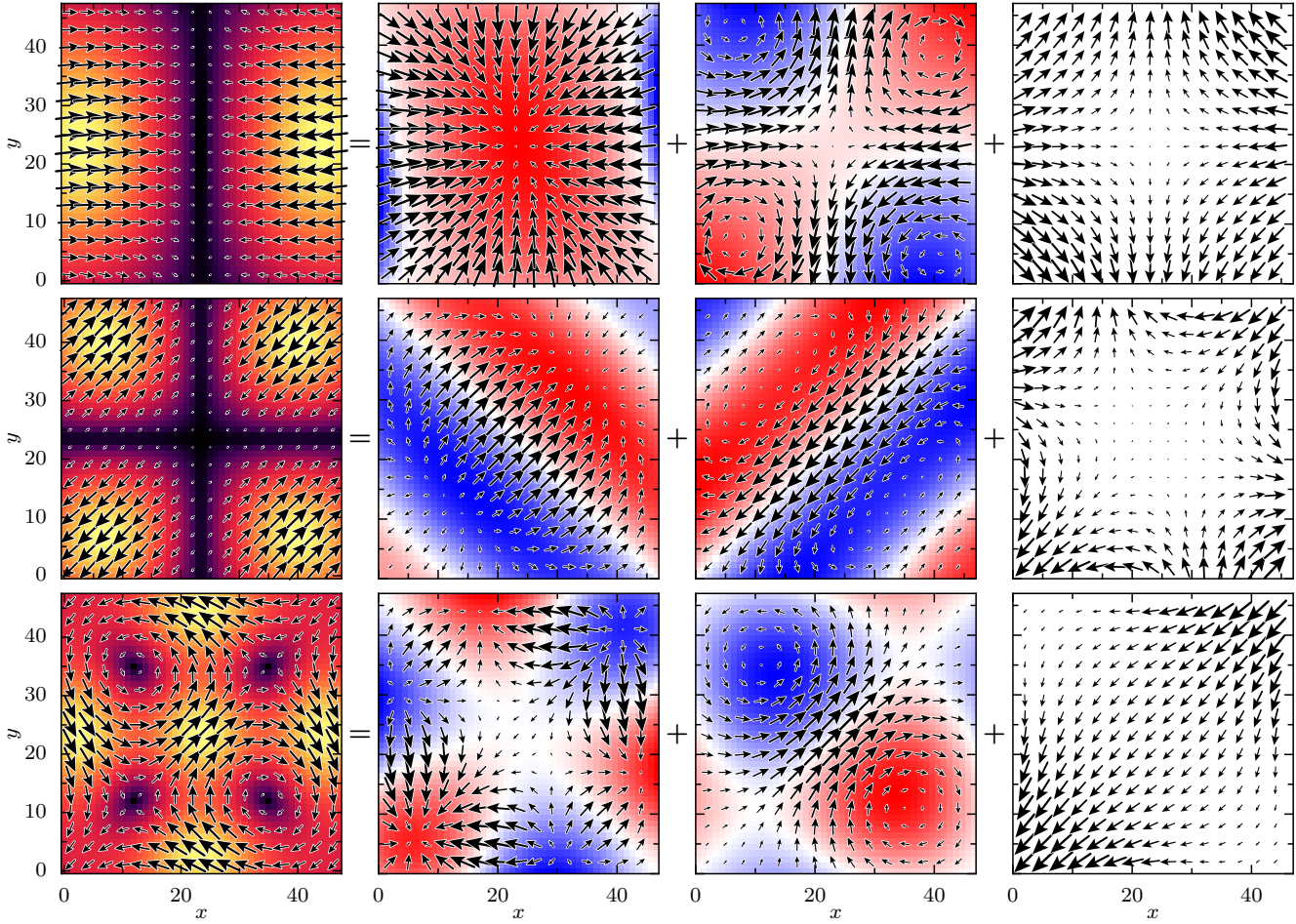


Figure 8 Three eigenmodes of the truncated system: Left panels show the displacement field, colours indicate absolute value (black=small, yellow=large). The three columns on the right show the Helmholtz–Hodge decomposition into longitudinal, transverse and harmonic parts. The blue/red colour shows the divergence (second column) and the rotation (third column) of the displacement field (red=negative, blue=positive). $\lambda = \mu$.

elastic medium, windowed to 48×48 in a system of dimensions 500×500 . Both the colour coding in black/yellow and the size of the arrows indicate the absolute value of the displacements. In these modes we find similar bow-shaped structures in the modes to those found in the scalar problem. It is interesting to note a number of properties of the figures. When we look at the distribution of amplitudes in the top panel, the maximum occurs at some distance from the edge of the sample and displays a vertical gradient in colour – this shows that despite the mode being largely longitudinal in nature it does display both longitudinal and transverse characters.

The longitudinal and transverse nature of these modes is better studied in an explicit Helmholtz–Hodge decomposition, which is displayed in the second to fourth columns of fig. 8. This requires some explanation. We want to split a vector field into a rotation-free part, $\nabla\phi$ and a divergence-free

part $\triangleright\psi$, with two scalar fields ϕ and ψ . The vector differential operator $\triangleright := (-\partial_y, \partial_x)^T$ replaces the **curl** in two dimensions[‡]. The rotation-free part should be “longitudinal”, and the divergence-free part “transverse”. However, this decomposition is unique only in infinite space. In the present case with a finite window, a third component \mathbf{h} may be required, having zero divergence and rotation. The decomposition then reads

$$\mathbf{u} = \nabla\phi + \triangleright\psi + \mathbf{h}. \quad (51)$$

After scalar multiplications with ∇ and with \triangleright , one finds that the scalars ϕ and ψ satisfy Poisson equations with divergence and rotation of the original field as sources,

$$\Delta\phi = \nabla \cdot \mathbf{u}, \quad \Delta\psi = \triangleright \cdot \mathbf{u}. \quad (52)$$

[‡] ψ can be considered the z component of the vector potential.

$\int \mathbf{u} ^2$	$\int \nabla\phi ^2$	$\int \triangleright\psi ^2$	$\int \mathbf{h} ^2$
1.00	0.42	0.04	0.25
1.00	0.30	0.29	0.19
1.00	0.02	1.06	0.42

Table 1 L_2 norms of the vector fields displayed in fig. 8, in the same order.

We now see that in the finite window the solutions to these equations are no longer unique but depend also on the boundary conditions we apply. One may obtain a possible decomposition into divergence-free and rotation-free parts by solving for ϕ with some boundary conditions imposed, e. g. Dirichlet or Neumann; the rest, $\mathbf{u} - \nabla\phi$ is then representable as $\triangleright\psi$. If specific boundary conditions are required also for ψ , then there is a third contribution \mathbf{h} which obeys the equation

$$\triangleright \cdot \mathbf{h} = \nabla \cdot \mathbf{h} = 0, \quad \Delta \mathbf{h} = \mathbf{0}. \quad (53)$$

In our case we lack a reasonable justification of such a boundary condition for ϕ or ψ , they give rise to visually unreasonable fields- for instance normal fluxes which are forced to zero at the edge of the box. We rather choose to come as close as possible to what we associate with “longitudinal” and “transverse” in the infinite system. We therefore do not impose a boundary conditions at the box edges but extend eqs. (52) to infinity by padding the right-hand sides with zero and requiring the solutions to vanish at infinity. The solution to this problem has already been discussed in sec. 4.1 and is the convolution of the right-hand sides of eq. (52) with minus the scalar Green function. The scalar fields ϕ and ψ contain the divergence and the rotation of the original field \mathbf{u} , and we believe that these solutions are the least perturbed by any boundary effects. The harmonic field \mathbf{h} is then simply what remains after subtraction of $\nabla\phi$ and $\triangleright\psi$.

The three contributions of eq. (51) are displayed in the three rightmost columns of fig. 8 (in the same order). The blue/red colour coding shows the right-hand sides of eqs. (52), red for negative values and blue for positive. In the second column, displaying $\nabla\phi$, we see how the arrows all head to the minima/maxima of the divergence field. In the second column, displaying $\triangleright\psi$, the arrows turn in positive or negative sense around the minima/maxima. The harmonic contribution in the third column has zero divergence and zero rotation. The arrows in all panels are scaled independently to best visualize the fields. For quantitative comparison we give the L_2 norms in table 1 [§]. One sees that the mode in the first row is mainly longitudinal, but that there is an important harmonic (quadrupolar) contribution. We found another mode of similar symmetry which was dominated by its transverse part (not

shown). The last line of the figure shows again a mainly transverse mode, but here the harmonic field is not quadrupolar but is of lower order than the dominant transverse part. Most interestingly, the middle row shows a mode where both longitudinal and transverse contributions are equally important. This shows clearly that the truncation mixes these two natures of the modes.

A numerical study of the scaling of the mode energies with size of the truncating box, ℓ confirmed that, as expected, eigenvalues scale as ℓ^2 ; thus Λ/ℓ^2 is the object which contains information about material properties. However we note that eq. (49) implies that in a disk geometry there can be a slow logarithmic cross-over for certain modes. One might expect similar logarithmic corrections in the square geometry too.

5 Conclusions

Data analysis, with both numerical and experimental data often require windowing. When correlation data is simply truncated it can lead to substantial artefacts in the measured amplitudes and can mislead as to the exact values of elastic constants. These errors can be considerably reduced by using windowing functions which decay faster in Fourier space. In particular we found that the Hann window gives good results.

The experimental analysis of windowed data also gives rise to interesting questions as to the nature of the observed eigenmodes. We have shown that the correlation functions give rise to problems which satisfy an interesting integral condition involving the correlation functions of the experimental system. We have made a study of the eigenvalue problem for scalar elasticity and showed how to find exact analytic solutions of the integral equation in spherical and circular geometries. In square geometries we exhibited eigenfunctions which deviate noticeably from plane waves. We note that the use of integral equations to characterize observed experimental correlations is known in field such as statistical analysis and atmospheric physics²².

A Elasticity with Gaussian window

We present here the calculation for a tensorial Green function in an isotropic three-dimensional medium, when analysed using Gaussian windowing. The longitudinal part of the Green function of the original system can be written in the form

$$G^{(l)}(\mathbf{k}) = \frac{1}{\lambda + 2\mu} \frac{|\mathbf{k}\rangle\langle\mathbf{k}|}{k^2}, \quad (54)$$

with unit column vectors $|\mathbf{k}\rangle = \mathbf{k}/k$ and their adjoint row vectors $\langle\mathbf{k}|$. The Gaussian weighting of eq. (16) involves only a single external vector quantity \mathbf{q} . Thus we can deduce that

$$(\lambda + 2\mu)G_w^{(l)}(\mathbf{q}, -\mathbf{q}) = A(q)\mathbf{I} + B(q)|\mathbf{q}\rangle\langle\mathbf{q}| \quad (55)$$

[§] The decomposition is not orthogonal so that the sum of the three individual terms is not unity

for two as yet unknown functions A and B . We note that this form involves both longitudinal and transverse parts in the new variables. We take the scalar product of eq. (54) and eq. (55) with \mathbf{q} and secondly study the trace of these equations to deduce that

$$A(q) + B(q) = \int |W(\mathbf{q} - \mathbf{k})|^2 \frac{(\hat{\mathbf{q}} \cdot \hat{\mathbf{k}})^2}{k^2} \frac{d\mathbf{k}}{(2\pi)^3} \quad (56)$$

$$3A(q) + B(q) = \int |W(\mathbf{q} - \mathbf{k})|^2 \frac{1}{k^2} \frac{d\mathbf{k}}{(2\pi)^3} \quad (57)$$

We perform the angular integrals, then recognize the radial integrals as being related to imaginary error functions:

$$A(q) + B(q) = \frac{1}{q^2} - e^{-\sigma^2 q^2} \frac{\sqrt{\pi} \operatorname{erfi}(\sigma q)}{2\sigma q^3} \quad (58)$$

$$3A(q) + B(q) = e^{-q^2 \sigma^2} \frac{\sqrt{\pi} \sigma}{q} \operatorname{erfi}(\sigma q) \quad (59)$$

The transverse part of the Green function

$$G_{ij}^{(t)}(\mathbf{k}) = \frac{\mathbf{I} - |\mathbf{k}\rangle\langle\mathbf{k}|}{\mu k^2} \quad (60)$$

also gives a contribution which can be expressed in terms of the functions A and B :

$$\mu G_w^{(t)}(\mathbf{q}, -\mathbf{q}) = (2A(q) + B(q))\mathbf{I} - B|\mathbf{q}\rangle\langle\mathbf{q}|. \quad (61)$$

The full Green function is then the sum of the contributions of eq. (55) and eq. (61).

When σq is large $A \approx 1/(\sigma^2 q^4)$, whereas $B(q) \approx 1/q^2$. Thus the reconstruction does not mix the longitudinal and transverse components of the response which are both found correctly. For intermediate values of σq , where A cannot be neglected, the transverse and longitudinal modes do mix, in a manner similar that we found with the small-wavevector reconstructions using the Hann window, Fig. 5. In particular the longitudinal stiffness is strongly underestimated. As a specific example we take $\lambda/\mu = 1$ and plot in Fig 9 the two effective values of ω as a function of σq .

Matching the mean squared width of a Hann window to a Gaussian gives $\sigma^2 = L^2(1/12 - 1/(2\pi^2))$, giving an approximate relation between our analytic calculations on Gaussian functions and practical windows in the experimental situation. For the first mode in a square sample for which $q = 2\pi/L$ we find $\sigma q \approx 1.1$.

References

- 1 A. Ghosh, V. K. Chikkadi, P. Schall, J. Kurchan and D. Bonn, *Phys. Rev. Lett.*, 2010, **104**, 248305.
- 2 A. Ghosh, R. Mari, V. Chikkadi, P. Schall, J. Kurchan and D. Bonn, *Soft Matter*, 2010, **6**, 3082–3090.

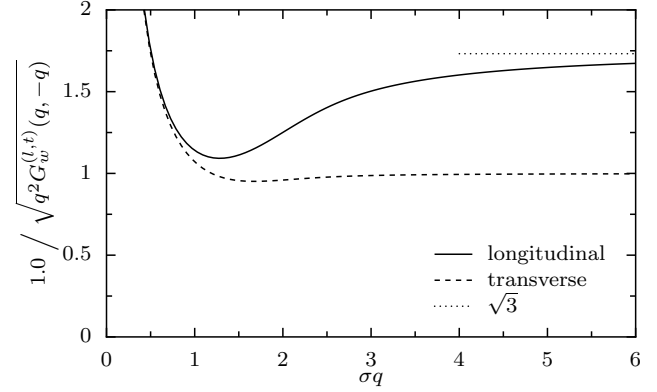


Figure 9 Effective ω/q as a function of σq for a three dimensional system with $\lambda/\mu = 1$, $\nu = 0$. For large values of σq the ratio of the two curves converges to $\sqrt{3}$. However mixing of the modes leads to a strong drop in the estimate of the longitudinal stiffness for $\sigma q \approx 1$.

- 3 A. Ghosh, R. Mari, V. Chikkadi, P. Schall, A. Maggs and D. Bonn, *Physica A: Statistical Mechanics and its Applications*, 2011, **390**, 3061 – 3068.
- 4 D. Kaya, N. L. Green, C. E. Maloney and M. F. Islam, *Science*, 2010, **329**, 656–658.
- 5 K. Zahn, A. Wille, G. Maret, S. Sengupta and P. Nielaba, *Phys. Rev. Lett.*, 2003, **90**, 155506.
- 6 C. A. Lemarchand, A. C. Maggs and M. Schindler, *ArXiv e-prints*, 2011.
- 7 P. Keim, G. Maret, U. Herz and H. H. von Grünberg, *Phys. Rev. Lett.*, 2004, **92**, 215504.
- 8 K. Chen, W. G. Ellenbroek, Z. Zhang, D. T. N. Chen, P. J. Yunker, S. Henkes, C. Brito, O. Dauchot, W. van Saarloos, A. J. Liu and A. G. Yodh, *Phys. Rev. Lett.*, 2010, **105**, 025501.
- 9 D. Reinke, H. Stark, H.-H. von Grünberg, A. B. Schofield, G. Maret and U. Gasser, *Phys. Rev. Lett.*, 2007, **98**, 038301.
- 10 H. Weyl, *Bull. Amer. Math. Soc.*, 1950, **56**, 115–139.
- 11 T. Itaka and T. Ebisuzaki, *Phys. Rev. E*, 2000, **61**, R3314–R3317.
- 12 D. C. Wallace, in *Thermoelastic Theory of Stressed Crystals and Higher-Order Elastic Constants*, ed. H. Ehrenreich, F. Seitz and D. Turnbull, Academic Press, New York and London, 1970, vol. 25, pp. 301–404.
- 13 M. Born and K. Huang, *Dynamical Theory of Crystal Lattices*, Oxford University Press, Oxford, 1998.
- 14 S. Pronk and D. Frenkel, *Phys. Rev. Lett.*, 2003, **90**, 255501.
- 15 L. Landau and E. Lifshitz, *Theory of Elasticity: Course of Theoretical Physics, volume 7, Ch. 1, Section 10.*, Butterworth-Heinemann, 1984.
- 16 A. Morawiec, *Phys. Stat. Sol (b)*, 1994, **184**, 313–324.
- 17 M. Schindler and A. C. Maggs, *Eur. Phys. J E*, 2011, **34**, 115.
- 18 D. C. Rapaport, *The art of molecular dynamics simulation*, Cambridge Univ. Press, 2nd edn., 2004.
- 19 A. H. Nuttall, *IEEE Transactions on Acoustics Speech and Signal Processing*, 1981, **29**, 84–91.
- 20 Y. H. Pao, *J. Acoust. Soc. Am.*, 1978, **64**, 302–310.
- 21 M. Abramowitz and I. A. Stegun, *Handbook of Mathematical Functions with Formulas, Graphs, and Mathematical Tables*, Dover, New York, ninth Dover printing, tenth GPO printing edn., 1964.
- 22 R. J. Mathar, *Baltic Astronomy*, 2008, **17**, 383–398.